CLIMATOLOGY

Changes in monsoon precipitation in East Asia under a 2°C interglacial warming

Xinbo Gao[1,2]*, Qingzhen Hao[2,3]*, Luo Wang[2,3], Yang Song[4], Junyi Ge[5], Haibin Wu[2,3], Bing Xu[2,3], Long Han[6], Yu Fu[2], Xuechao Wu[7], Chenglong Deng[8,3], Zhengtang Guo[2,3]

Past intervals of warming provide the unique opportunity to observe how the East Asia monsoon precipitation response happened in a warming world. However, the available evaluations are primarily limited to the last glacial-to-interglacial warming, which has fundamental differences from the current interglacial warming, particularly in changes in ice volume. Comparative paleoclimate studies of earlier warm interglacial periods can provide more realistic analogs. Here, we present high-resolution quantitative reconstructions of temperature and precipitation from north-central China over the past 800 thousand years. We found that the average precipitation increase, estimated by the interglacial data, was only around one-half of that estimated for the glacial-to-interglacial data, which is attributed to the amplification of climate change by ice volume variations. Analysis of the interglacial data suggests an increase in monsoon precipitation of ~100 mm for a warming level of 2°C on the Chinese Loess Plateau.

INTRODUCTION

Evaluating changes in regional climate at specific levels of warming, especially given the Paris Agreement target of 2°C warming (*1*), has been motivated by the growing perceived threat from global warming (*2*, *3*). The East Asian summer monsoon circulation is a key component of global hydroclimatic cycles, and monsoon precipitation variability directly affects the lives of more than 20% of the world's population. Thus, improved insights into changes in monsoon precipitation under a 2°C warming scenario in East Asia are urgently needed.

Climate changes during warm intervals in the geological past offer a broad set of natural experiments, in which the Earth system operated within a warming world (*4*–*7*). Our current understanding of monsoon precipitation changes under warm climate states primarily relies on the last full glacial-to-interglacial warming (here termed "G-to-IG warming"). Previous studies focusing on this warming transition using proxy-based reconstructions from cave stalagmites (*8*), loess deposits (*9*), lake sediments (*10*), and climate model simulations (*11*) suggest the northwestward migration of the monsoon rainfall belt by hundreds of kilometers, although the magnitude of the migration varies considerably between studies. However, the last G-to-IG warming has fundamental differences from the current interglacial warming. Under the current global warming, the Arctic region will experience the shrinking of the Greenland ice sheet and even ice-free conditions. However, the last G-to-IG warming represents a climate transition from a full glacial state to a full interglacial state, in which climate changes were induced by large fluctuations in Arctic ice volume (with the latitudinal displacement of climate regimes) (*12*), rather than an increase in temperature alone. Therefore, a comparative study of climate changes among warm interglacial periods (here termed "IG-to-IG warming," referring to climate changes within interglacial context, which are obtained by the climate comparison of different interglacials) can potentially offer a closer analog for warming over the next century. The preferred interval for this study includes a series of interglacials over the past 800 thousand years (ka) with different levels of warming and almost the same continental configuration as today (*13*).

Evaluating changes in monsoon precipitation at a specific warming level also depends critically on reliable quantitative reconstructions of East Asian continental air temperature and monsoon precipitation. The loess-paleosol sequences of the Chinese Loess Plateau (CLP) are valuable archives of the East Asian monsoon climate (*14*, *15*). Numerous studies have shown that paleoprecipitation can be quantitatively reconstructed based on multiple proxies such as magnetic susceptibility (*16*), cosmogenic ^{10}Be (*17*, *18*), and various carbonate-related proxies (*19*–*21*). However, the available proxies for paleotemperature reconstruction are scarce. In the past decade, proxies based on branched glycerol dialkyl glycerol tetraether (brGDGT) membrane lipids of soil-dwelling bacteria have been widely used in air temperature reconstructions based on loess deposits (*22*–*25*). However, the latest research indicates that brGDGTs mainly reflect the soil temperature rather than the air temperature (*26*, *27*). Thus, it is imperative to explore alternative and more dependable paleotemperature proxies for loess studies.

Pedogenic hematite holds great promise for quantifying the paleotemperature of loess (*28*, *29*). The reddish color of soil units in loess-soil couplets originates mainly from the pedogenic formation of pigmentary hematite during past warm periods. Recently, our detailed magnetic investigations of a large suite of modern soils (180 samples) from the CLP (Fig. 1) demonstrated that the formation of hematite during pedogenesis is dominantly controlled by the variation of the ambient temperature (*30*).

[1]State Key Laboratory of Earthquake Dynamics, Institute of Geology, China Earthquake Administration, Beijing 100029, China. [2]Key Laboratory of Cenozoic Geology and Environment, Institute of Geology and Geophysics, Chinese Academy of Sciences, Beijing 100029, China. [3]University of Chinese Academy of Sciences, Beijing 101408, China. [4]Beijing Academy of Science and Technology, Beijing 100089, China. [5]Key Laboratory of Vertebrate Evolution and Human Origins, Institute of Vertebrate Paleontology and Paleoanthropology, Chinese Academy of Sciences, Beijing 100044, China. [6]School of Ecology and Environmental Science, Zhengzhou University, Zhengzhou 450001, China. [7]School of Ocean and Earth Science, Tongji University, Shanghai 200092, China. [8]State Key Laboratory of Lithospheric Evolution, Institute of Geology and Geophysics, Chinese Academy of Sciences, Beijing 100029, China.
*Corresponding author. Email: xinbo-gao@outlook.com (X.G.); haoqz@mail.iggcas.ac.cn (Q.H.)

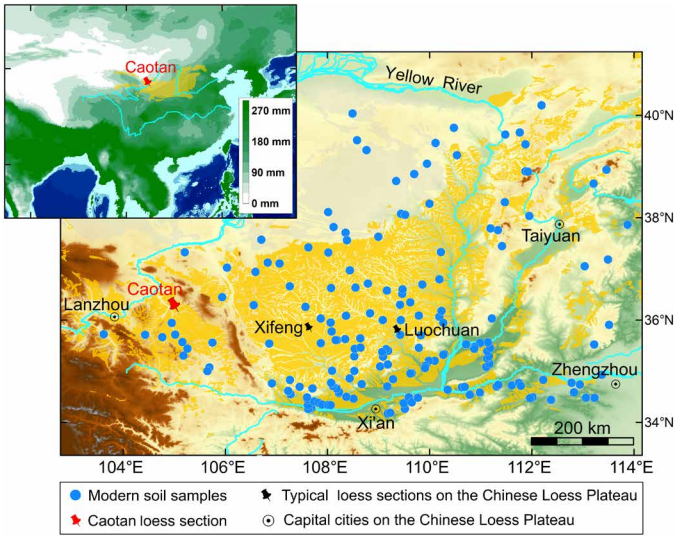

Fig. 1. Locations of modern soil samples and the Caotan loess section on the CLP. Blue dots denote 180 modern soil samples from the CLP and adjacent areas. The red pushpin indicates the Caotan loess profile located in the northwestern part of the CLP. The black pushpins indicate the typical loess sections on the CLP. The circles with central dots are major cities. The inset map in the top left corner shows the location of the study area within East Asia and the mean July precipitation (green contours) [precipitation data from the dataset of spatially interpolated monthly climate data for global land areas at a 1-km spatial resolution (*67*)].

Here, we studied the environmental magnetic properties, diffuse reflectance spectroscopy (DRS), and iron geochemistry (see text S1) on the same suite of modern soils (*30*), to create a hematite-temperature climofunction. Then, the established paleotemperature and paleoprecipitation climofunctions were applied to a thick loess-paleosol sequence (the Caotan section, 105°9′E, 36°14′N) on the western Loess Plateau (Fig. 1). The Caotan section lies in the marginal area of modern monsoon rainfall and hence is sensitive to past variations in monsoon strength. This section also has a high dust sedimentation rate and hence a superior stratigraphic resolution of warm climate events compared to loess sections in the eastern region, e.g., three sub-paleosol units are clearly identified within paleosol S1 (*31*), correlated to marine oxygen isotope stages (MIS) 5a, 5c, and 5e. The quantitatively estimated temperature and precipitation spanning the past 800 ka enable us to statistically evaluate the changes in monsoon precipitation under different warming contexts (IG-to-IG warming and G-to-IG warming). Here, we address the changes in monsoon precipitation at a warming level of 2°C over northwestern China for the IG-to-IG warming and evaluate its differences to the G-to-IG warming.

RESULTS AND DISCUSSION

Climofunctions for quantifying temperature and precipitation

DRS and iron geochemistry evidence further verify that hematite can be used in paleotemperature reconstructions based on Chinese loess. The spatial distribution of hematite content on the CLP is characterized by a steep gradient of increasing hematite concentration from 0.94 g/kg in the northwestern Loess Plateau to 6.52 g/kg in the southeastern Loess Plateau (Fig. 2A). The closely spaced contours in the southeastern and southwestern Loess Plateau and the relatively sparse contours in the northcentral Loess Plateau closely track changes in the modern observed temperature, which confirms the strong linkage between soil hematite content and temperature. Regression analysis further demonstrates that the correlation between hematite content and temperature ($R^2 = 0.62$; R is the correlation coefficient) is greater than that with precipitation ($R^2 = 0.48$) (Fig. 2, B and C). The strong linear relationship between hematite content and temperature enabled us to use a least squares regression model to build the following annual temperature (T_A) versus hematite content ($Hem_{content}$) climofunction: T_A °C/year = 1.80*($Hem_{content}$ g/kg) + 3.84 ($n = 180$, S.E. = 1.54°C, and $P < 0.0001$).

The dominant control of temperature on hematite formation is mainly via its influence on the transformation of iron oxides/hydroxides and on the content of soil organic matter. First, an enhanced temperature will directly promote the formation of hematite. It is widely recognized that hematite forms mainly by the thermal transformation of various Fe hydroxides, such as goethite, ferrihydrite, and feroxyhyte, via dehydroxylation and internal reorganization (*29*). Recently, a series of in vitro experiments confirmed that a major transformation pathway in soils is from ferrihydrite to hydromaghemite to hematite (*32*–*34*). In addition, the oxidation of magnetite and thermal decomposition of Fe salts and chelates also contribute to the production of hematite (*28*). It has been demonstrated that higher ambient temperatures will promote thermal transformation, dehydroxylation, and decomposition processes and favor the accumulation of hematite, as supported by in vitro experiments (*32*–*34*). Second, temperature affects the formation of hematite by adjusting the concentration of organic matter. In soils, organic matter is an excellent complexing agent, which usually lowers the activity of Fe^{3+}, in turn suppressing the formation of ferrihydrite, the precursor of hematite (*29*). In addition, higher organic matter content may also result in a reduced soil environment, in which hematite will be dissolved preferentially (*28*). The enhanced temperature will promote the decomposition of organic matter, thereby favoring the accumulation of the precursor ferrihydrite and hematite.

Precipitation also plays a role in the formation of hematite. For the production of iron oxides or hydroxides in soils, the prerequisite is the free Fe^{2+} released by the weathering of iron-containing silicates, which is strongly dependent on both moisture and temperature. In the East Asian monsoon region, the changes in temperature and precipitation are roughly in phase. Thus, it is easy to understand the moderate correlation between precipitation and hematite content (Fig. 2C).

However, temperature plays a leading role in the formation of hematite. Our previous redundancy analyses between the magnetic parameters of modern soils from the CLP and instrumentally recorded climate variables (*30*) showed that hematite formation is controlled mainly by ambient temperature rather than by precipitation. Therefore, hematite is a promising paleotemperature proxy and can be reliably applied in the quantitative estimation of the paleotemperature of Chinese loess.

Magnetic susceptibility is a widely accepted proxy for the strength of the East Asian summer monsoon (*16*, *35*). Here, as reported in previous studies (*30*, *36*), the spatial pattern of the frequency-dependent magnetic susceptibility (χ_{fd}) across the CLP is strongly correlated with the modern observed precipitation gradient, characterized by gradually increasing χ_{fd} and precipitation values from the

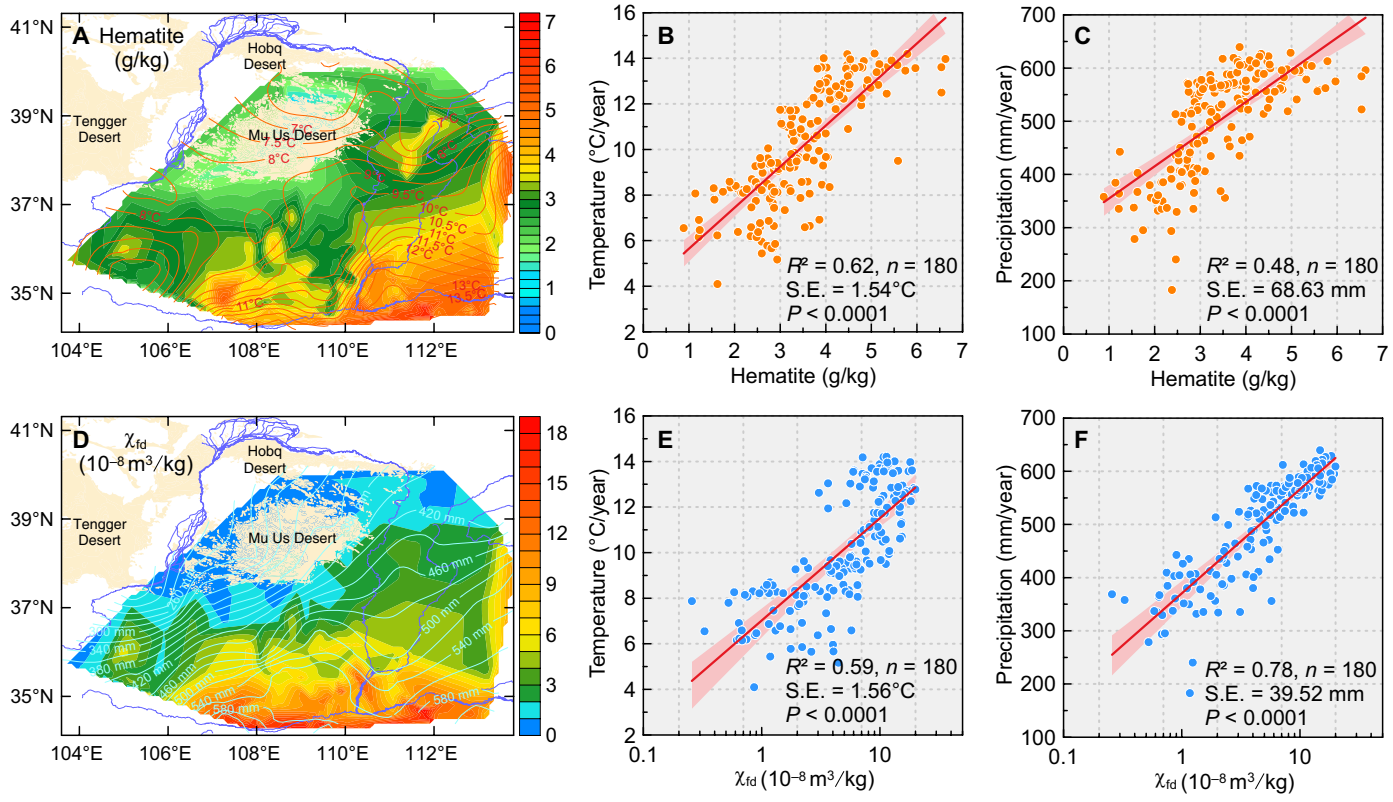

Fig. 2. Spatial distribution of the hematite content and frequency-dependent magnetic susceptibility (χ_{fd}) of modern soils on the CLP and their correlations with observed temperature and precipitation. (**A**) Contour maps of hematite content (filled contours) and modern observed temperature (red contours). (**B** and **C**) Least squares regression (red line) between hematite content and temperature and precipitation; red shaded areas indicate 95% confidence intervals estimated using the Student's *t* test. (**D**) Contour maps of χ_{fd} (filled contours) and modern observed precipitation (blue contours). (**E** and **F**) Least squares regression (red line) between χ_{fd} and temperature and precipitation; red shaded areas indicate 95% confidence intervals estimated using the Student's *t* test.

northern Loess Plateau to the southern Loess Plateau (Fig. 2D). The higher correlation between ln(χ_{fd}) and precipitation (R^2 = 0.78) than that between χ_{fd} and temperature (R^2 = 0.59) provides statistical confirmation that χ_{fd} is specifically sensitive to the variation of precipitation (Fig. 2, E and F). Accordingly, we used the 180 modern soil samples to develop the following ln(χ_{fd}) versus annual precipitation (P_A) climofunction: P_A mm/year = 85.00*ln(χ_{fd} 10^{-8} m^3/kg) + 370.34 (n = 180, S.E. = 39.52 mm, and P < 0.0001).

Direct application of temperature or precipitation climofunctions may lead to biased estimates of paleoclimate variables (text S2) because of substrate differences between modern soils and paleosols. However, the slope of the climofunction provides reliable information about temperature-induced and precipitation-induced changes in $Hem_{content}$ and ln(χ_{fd}), respectively. Thus, following the strategy of temperature reconstructions used for the Dome C ice core from Antarctica (*37*), we use the slope of the climofunction [T_A °C /year = 1.80*($Hem_{content}$ g/kg) + 3.84 and P_A mm/year = 85.00*ln(χ_{fd} 10^{-8} m^3/kg) + 370.34] to calculated changes in temperature (T_{change}) and precipitation (P_{change}) relative to the late Holocene, respectively. In our reconstruction, records of $\Delta Hem_{content}$ and Δln(χ_{fd}) for the Caotan section were obtained with respect to the mean $Hem_{content}$ and χ_{fd} values over the past 3 ka, and then the equations T_{change} = 1.80*$\Delta Hem_{content}$ and P_{change} = 85.00*Δln(χ_{fd}) were used to calculate changes in temperature and precipitation on the CLP (Fig. 3).

Temperature and precipitation variations over the past 800 ka

The temporal changes in the reconstructed temperature and precipitation of the Caotan section over the past 800 ka show clear orbital-scale variability (Fig. 3). Eight glacial-interglacial cycles are evident in the temperature and precipitation records and both records contain the periodicities of 100 ka, 41 ka, and 23 ka (fig. S7), confirming the role of Earth orbital variations in driving monsoon climate changes. The interglacial intervals are generally characterized by warm and humid conditions and the glacial intervals by cold and dry conditions. Consistent with global paleoclimate records (*13*), MIS 5e and MIS 11c were especially strong interglacials, characterized by higher temperatures and precipitation (Fig. 3, B and C), compared with the other interglacials over the past 800 ka.

Comparison between the estimated temperature and precipitation records reveals a clear difference in the long-term trend of variation. Over the last 800 ka, the precipitation record shows a greatly increased amplitude for interglacials after ~424 ka, coinciding with the Mid-Brunhes Event (MBE) (*38*–*40*). However, the pre- and post-424-ka temperature records show an overall constant amplitude during interglacials. A similar pattern was reported in a global stacked sea surface temperature record (*41*) and a biogenic silica record from Lake Baikal (fig. S8) (*42*). The contrasting patterns of temporal variations between the temperature and precipitation records

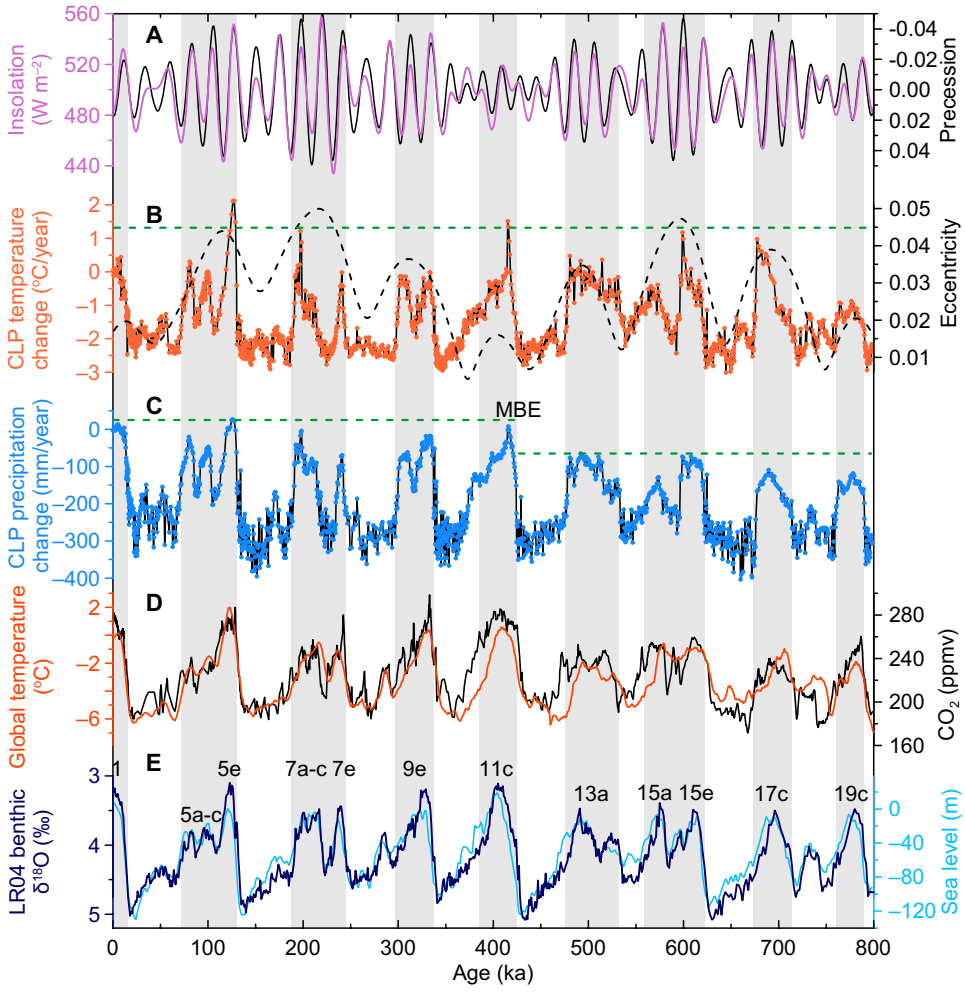

Fig. 3. Comparison of reconstructed temperature and precipitation for the Caotan section with other palaeoclimate records over the past 800 ka. (**A**) June insolation 65°N (violet line) and Earth orbital precession (black line) (*68*). (**B**) Hematite-based temperature record of the Caotan loess/paleosol sequence (orange dots) and Earth orbital eccentricity (black trace) (*68*). (**C**) Frequency-dependent magnetic susceptibility (χ_{fd})–based precipitation record of the Caotan section (blue dots). (**D**) Global temperature (red line) (*45*) and atmospheric CO_2 concentration (black line) (*69*). (**E**) Benthic $\delta^{18}O$ stack LR04 (dark blue line) (*70*) and a stacked sea-level record (light-blue line) (*71*) (numbers indicate marine isotope stages). The shaded areas indicate major interglacial intervals and their correlation with other palaeoclimatic records.

suggest that they have evolved relatively independently and have different driving mechanisms.

The hematite-based temperature record also shows distinct differences compared to temperature records derived from Phytolith and brGDGTs (fig. S10). Most notable are the different patterns of variation in the glacial and interglacial cycles. The hematite-based temperature record of the Caotan section, phytolith-based temperature record of the Weinan section (*43*), and brGDGTs-based temperature records from the Weinan and Mangshan sections (*24*, *44*) all show warmer interglacial periods and colder glacial periods—i.e., a similar pattern to that of global air temperature over the past 800 ka (*45*). By contrast, the brGDGTs-based temperature records from the Xifeng and Luochuan sections show warmer conditions in several glacial periods and colder conditions in a few interglacial periods (*26*). The contrasting patterns observed in brGDGTs-based temperature records highlight the complexity of the response of soil bacteria to pedogenic conditions.

Encouragingly, our χ_{fd}-based precipitation record for the Caotan section closely tracks the variability in the ^{10}Be-based rainfall record of the past 600 ka from the Baoji section (fig. S11) (*18*), reinforcing the reliability of our reconstruction. The strong correlation between these two records also underscores the conclusion that the χ_{fd} of loess deposits on the CLP is a dependable proxy for monsoon precipitation reconstruction, at least over the past 800 ka.

Response of monsoon precipitation to 2°C of interglacial warming

We used regression analyses to estimate changes in monsoon precipitation at specific levels of warming (mainly 2°C in the present study). Our independent temperature and precipitation data from the same record enabled us to directly compare these two datasets. We regressed the reconstructed precipitation records versus the reconstructed temperature records for the IG-to-IG warming and G-to-IG warming, respectively. For the IG-to-IG warming, only interglacial

data were used for the calculation (Fig. 4, D to F), and for the G-to-IG warming, all the glacial and interglacial data were used (Fig. 4, A to C). Considering the possible influence of human activities on the Holocene soils of the CLP (*46*), data for the past 12 ka were removed from the analyses. For all time intervals (Fig. 4, A to F), precipitation generally increased as a positive linear function of temperature. Accordingly, linear regressions were performed and the regression slopes describe the average precipitation increment ΔP per degree centigrade.

Our analyses reveal that the average precipitation increment per degree centigrade for the IG-to-IG warming is approximately one-half of that estimated from the G-to-IG warming. For the G-to-IG warming (Fig. 4, G to I), the average precipitation changes (ΔP) are higher, with 91.97 mm/°C for the entire time series (800 ka to 12 ka), 102.5 mm/°C for the interval of 424 ka to 12 ka, and 77.36 mm/°C for the interval of 800 ka to 424 ka. Comparatively, the average ΔP values for the IG-to-IG warming (Fig. 4, G to I) are lower and relatively stable, with 48.19 mm/°C for the entire time series (800 ka to 12 ka), 49.6 mm/°C for the interval of 424 ka to 12 ka, and 40.48 mm/°C for the interval of 800 ka to 424 ka. The average precipitation increment per degree centigrade is approximately twice that for the G-to-IG warming compared to the IG-to-IG warming.

The different magnitude of precipitation increment between these two warming cases highlights the profound impacts of large-scale Northern Hemisphere ice retreat under the G-to-IG warming,

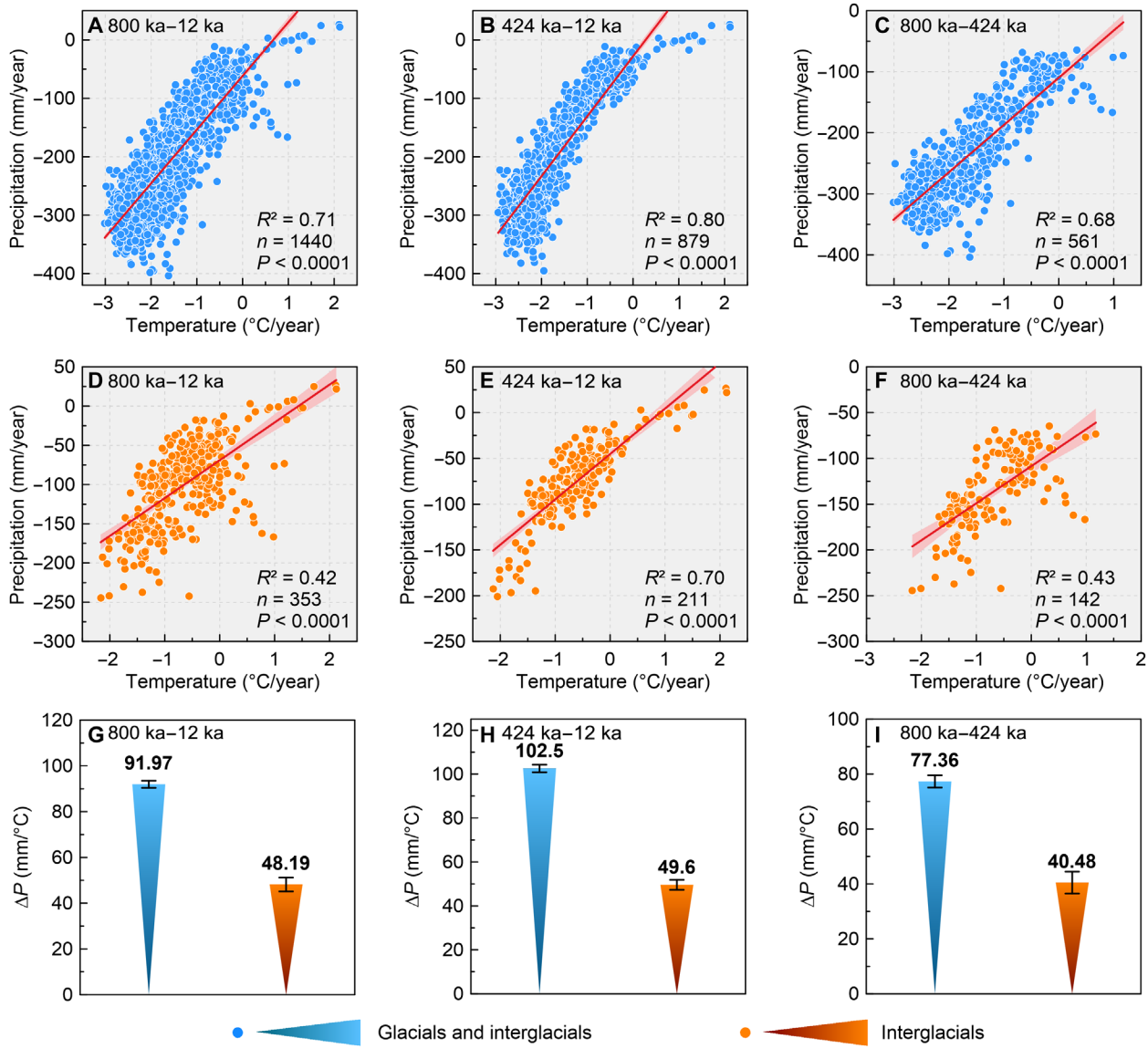

Fig. 4. Results of statistical analysis of the reconstructed temperature and precipitation data for different climatic stages and time intervals. (**A** to **C**) Cross plots of the reconstructed temperature and precipitation of glacials and interglacials for different time intervals. (**D** to **F**) Cross plots of the reconstructed temperature and precipitation of interglacials for different time intervals. In all panels, red lines represent the least squares regression line and the red shaded areas represent 95% confidence intervals estimated using the Student's *t* test. (**G** to **I**) Average precipitation increments (ΔP) per degree centigrade of the glacial-interglacial warming and that of the interglacial warming for different time intervals; solid ticks indicate the error bars.

relative to the IG-to-IG warming. For the G-to-IG warming, the higher ΔP for the interval of 424 ka to 12 ka (102.5 mm/°C; Fig. 4H) compared to the interval of 800 ka to 424 ka (77.36 mm/°C; Fig. 4I) also supports the strong impact of ice sheets on monsoon precipitation, as the ice volume variability was greater after the MBE (*38*–*40*).

The G-to-IG warming in the geological past involved substantial changes in ice cover outside Greenland, including in much of northern Eurasia and North America, namely, the Scandinavian ice sheet and Laurentide ice sheet, which were several times larger than the present-day Greenland ice sheet (Fig. 3E) (*47*). It is widely recognized that changes in Arctic ice sheets amplify climate changes via their direct and indirect influences on sea surface temperature, ocean circulation, continental water balance, vegetation, and land surface albedo (*47*). For the East Asian summer monsoon, the environmental effects of changes in Arctic ice sheets can be summarized as follows. First, the growth and decay of Arctic ice sheets and the associated sea level variations would have led to the exposure and submergence of extensive continental shelf regions of the East Asian continent (*48*). These large changes in the land-sea configuration (*12*) would, in turn, have influenced land-ocean thermal gradients and distance to the oceanic moisture sources (*46*, *49*, *50*). Second, the waxing and waning of Arctic ice sheets would also have resulted in substantial latitudinal movement of the atmosphere system. The latest proxy-simulation syntheses suggest that continental ice sheets alter the meridional temperature gradient, resulting in the 2° to 3° equatorward migration of the high-level westerlies (*51*, *52*), and, in turn, a weaker and southward shift of the monsoon precipitation over the East Asian continent (*53*). Third, as one of the largest topographic features on Earth, Arctic ice sheets have a large effect on the monsoon climate via their influence on the regional albedo and radiation balance (*47*). Fourth, Arctic ice volume variations also have a large effect on the monsoon rainfall budget of East Asia via the direct modulation of sea surface temperature and evaporation over the Western Pacific Ocean (*18*). Therefore, the East Asian summer monsoon changes from full glacial to full interglacial conditions are the result of changes in both ice volume and temperature, inevitably resulting in the overestimation of the magnitude of the precipitation increment.

The past interglacial warming provides a more realistic analog for future warming regarding changes in the volume of Arctic ice. Studies of the history of the Greenland ice sheet suggest that the warmer interglacial intervals over the past 800 ka include several warming cases that may apply in the future. In the case of MIS 5e and 9e, the ice cover on southern Greenland was likely limited, while in MIS 11c, ice was almost absent from Greenland (*54*–*57*). Consistent with the global paleoclimate reconstructions (*13*), our results also suggest that MIS 5e and MIS 11c provide a closer analog for future warming (Fig. 3). The estimated average precipitation changes (ΔP) is 41.92 mm/°C for MIS 5e and MIS 11c ($n = 52$) (fig. S12), close to the statistical estimates of the precipitation and temperature of the last four pre-Holocene interglacials ($\Delta P = 49.6$ mm/°C) (Fig. 4H). Statistically, the larger dataset of the last four pre-Holocene interglacials ($n = 211$) is more preferable (Fig. 4E), and it may provide more reliable constraints on changes in monsoon precipitation for the warming over the next century. Therefore, our results suggest that under a 2°C interglacial warming, monsoon precipitation over northwestern China will increase by ~99.2 mm (Fig. 4H).

This estimate is generally consistent with climate modeling results. Climate model simulations project that the average precipitation in China would increase by 5 to 20% under the Representative Concentration Pathways 4.5 (RCP4.5) scenario, and by 12 to 39% under the RCP8.5 scenario by the end of this century (*58*–*62*). Specifically, for the present study site, precipitation would increase by 17.95 to 71.80 mm and 43.08 to 140.01 mm under the RCP4.5 and RCP8.5 scenarios, respectively. Overall, our results provide potentially more dependable constraints for future climate modeling studies.

In summary, the present study has evaluated the influence of climate warming on East Asian summer monsoon precipitation using quantitative data for interglacials over the past 800 ka. We found that the magnitude of the precipitation increment was only around one-half of the estimates based on studies of the last glacial-to-interglacial warming, in which the influence of large-scale ice volume retreat alone cannot be excluded. The past interglacial warming, characterized by a limited ice cover in Greenland, offers a closer analog for future warming and thus a potentially more reliable estimate and constraint for model simulations.

MATERIALS AND METHODS

General settings and sampling

Modern soils on the CLP are typically developed within the uppermost loess unit L0. In field sampling, leaves, roots, and small stones were first removed, and then samples from ~2 to 5 cm beneath the surface were collected. To avoid potential contamination from modern human activities, sampling sites were usually located far from cultivated land, urban and industrial areas, and major roads. In this study, a total of 180 modern soil samples were collected from across the CLP and adjacent areas. These samples cover a present-day observed precipitation gradient from 150 mm on the northwestern Loess Plateau to 700 mm on the southeastern Loess Plateau and an observed north-to-south temperature gradient from 6° to 13°C.

The Caotan section is located in Caotan town, Huining County, in the northwestern part of the CLP. The modern observed mean annual precipitation and temperature are ~359 mm and ~ 8.5°C, respectively. Loess deposits in the northwestern part of the CLP are usually characterized by higher sedimentation rates. In the Caotan section, the thickness of the loess deposits, spanning the past 800 ka, is 103.8 m, including loess units L1 to L7 and paleosol units S0 to S7. In the field, a total of 4152 powder samples were collected at a sampling interval of 2.5 cm; among them, 1519 samples were selected for analysis at 5-cm intervals for paleosol units and 10-cm intervals for loess units, representing an approximate mean temporal resolution of ~500 years per sample.

Chronology

The chronological framework of the Caotan section was generated using the widely accepted grain size–based age model (*46*, *63*)

$$T_m = T_1 + (T_2 - T_1)\left(\sum_{i=1}^{m} A_i^{-1}\right)\left(\sum_{i=1}^{n} A_i^{-1}\right)^{-1}$$

where T_1 and T_2 are the age control points; A_i represents the accumulation rate at level i, which is assumed to be proportional to the content of particles larger than 32 μm (*46*); n represents the total sampling level between T_1 and T_2; and m represents the sampling level at T_1 and T_2. Absolute age control points are established on the basis of the well-established correlation scheme between

loess-paleosol sequences and marine records (*21*, *46*). It is commonly considered that loess units formed during glacials with a strengthened East Asian winter monsoon, and paleosol units formed during interglacials with a strengthened East Asian summer monsoon (*14*). The chronology between age control points was derived via interpolation weighted by the content of >32-μm particles (*46*).

Magnetic susceptibility

Low- and high-frequency magnetic susceptibility (χ_{lf} and χ_{hf}) were measured on air-dried powder samples, using a Bartington MS3 magnetic susceptibility meter with an MS2B dual-frequency sensor at 470 and 4700 Hz, respectively. Frequency-dependent susceptibility (χ_{fd}), which is a widely accepted indicator of the strength of the East Asian summer monsoon, is calculated as the difference between χ_{lf} and χ_{hf}.

Diffuse reflectance spectroscopy

DRS spectra of 0.5 g of finely powdered samples were generated using a Varian Cary 5000 ultraviolet-visible-infrared spectrophotometer with a wavelength range from 300 to 700 nm, scan rate of 300 nm/min, and scan step of 0.5 nm. The raw DRS data were smoothed and transformed to the Kubelka-Munk remission function [$F(R) = (1 - R)^2/2R$], and then the second derivative spectrum was calculated. It is widely documented that the band intensities at ~425 and ~535 nm in the second derivative curves ($I_{425\ nm}$ and $I_{535\ nm}$) are proportional to the concentrations of fine-grained pigmentary goethite and hematite, respectively (*64*).

Free iron oxides

Free iron oxides (Fed) represent the iron liberated from the silicate minerals by weathering and were used to evaluate the total concentrations of hematite and goethite. Fed was determined with the citrate-bicarbonate-dithionite method (*65*). A precisely weighed amount of finely ground sample (0.1 g) was placed in a 50-ml centrifuge tube and 0.15 g of solid $Na_2S_2O_4$, 4.0 ml of 0.3 mol Na-citrate solution, and 0.5 ml of 1.0 mol $NaHCO_3$ solution were added. The digest was then heated at 75°C for 15 min in a water bath, stirring occasionally. The suspension was centrifuged for 3 min at 4000 rpm. Last, 0.5 ml of clear supernatant was removed with a pipetting gun and decanted into a 100-ml volumetric flask, and the solution was retained for Fe determination. The iron concentration was measured using a PerkinElmer PinAAcle 900 T flame atomic absorption spectrometer, and replicate analyses ($n = 3$) show that the standard deviation is <0.01.

Spectral analysis

Spectral analyses of the reconstructed temperature, precipitation, benthic $\delta^{18}O$, CO_2, insolation, and eccentricity were conducted using Past3 software (*66*). The REDFIT program was used to identify the primary astronomical components. The 95% confidence line is used to assess the reliability of the results.

Meteorological data

Modern observed temperature and precipitation data for a 40-year interval (1951–1990) were obtained from the China Meteorological Administration. For each sampling site of modern soil, temperature and precipitation data were generated using inverse-distance weighting spatial interpolation.

Supplementary Materials

This PDF file includes:

Supplementary Texts S1 and S2
Figs. S1 to S12
References

REFERENCES AND NOTES

1. Paris Agreement, in *Report of the Conference of the Parties to the United Nations Framework Convention on Climate Change, 2015*, retrieved December (HeinOnline, 2015), vol. 4, p. 2017.
2. Z. Hausfather, K. Marvel, G. A. Schmidt, J. W. Nielsen-Gammon, M. Zelinka, Climate simulations: Recognize the 'hot model' problem. *Nature* **605**, 26–29 (2022).
3. P. Voosen, 'Hot' climate models exaggerate Earth impacts. *Science* **376**, 685–685 (2022).
4. J. C. Zachos, G. R. Dickens, R. E. Zeebe, An early Cenozoic perspective on greenhouse warming and carbon-cycle dynamics. *Nature* **451**, 279–283 (2008).
5. M. A. Martínez-Botí, G. L. Foster, T. B. Chalk, E. J. Rohling, P. F. Sexton, D. J. Lunt, R. D. Pancost, M. P. S. Badger, D. N. Schmidt, Plio-Pleistocene climate sensitivity evaluated using high-resolution CO_2 records. *Nature* **518**, 49–54 (2015).
6. H. Fischer, K. J. Meissner, A. C. Mix, N. J. Abram, J. Austermann, V. Brovkin, E. Capron, D. Colombaroli, A. Daniau, K. A. Dyez, T. Felis, S. A. Finkelstein, S. L. Jaccard, E. L. McClymont, A. Rovere, J. Sutter, E. W. Wolff, S. Affolter, P. Bakker, J. A. Ballesteros-Cánovas, C. Barbante, T. Caley, A. E. Carlson, O. Churakova, G. Cortese, B. F. Cumming, B. A. S. Davis, A. D. Vernal, J. Emile-Geay, S. C. Fritz, P. Gierz, J. Gottschalk, M. D. Holloway, F. Joos, M. Kucera, M. Loutre, D. J. Lunt, K. Marcisz, J. R. Marlon, P. Martinez, V. Masson-Delmotte, C. Nehrbass-Ahles, B. L. Otto-Bliesner, C. C. Raible, B. Risebrobakken, M. F. Sánchez Goñi, J. S. Arrigo, M. Sarnthein, J. Sjolte, T. F. Stocker, P. A. Velasquez Alvárez, W. Tinner, P. J. Valdes, H. Vogel, H. Wanner, Q. Yan, Z. Yu, M. Ziegler, L. Zhou, Palaeoclimate constraints on the impact of 2°C anthropogenic warming and beyond. *Nat. Geosci.* **11**, 474–485 (2018).
7. J. E. Tierney, C. J. Poulsen, I. P. Montanez, T. Bhattacharya, R. Feng, H. L. Ford, B. Honisch, G. N. Inglis, S. V. Petersen, N. Sagoo, C. R. Tabor, K. Thirumalai, J. Zhu, N. J. Burls, G. L. Foster, Y. Godderis, B. T. Huber, L. C. Ivany, S. Kirtland Turner, D. J. Lunt, J. C. McElwain, B. J. W. Mills, B. L. Otto-Bliesner, A. Ridgwell, Y. G. Zhang, Past climates inform our future. *Science* **370**, eaay3701 (2020).
8. W. S. Broecker, A. E. Putnam, Hydrologic impacts of past shifts of Earth's thermal equator offer insight into those to be produced by fossil fuel CO_2. *Proc. Natl. Acad. Sci. U.S.A.* **110**, 16710–16715 (2013).
9. S. L. Yang, Z. L. Ding, Y. Y. Li, X. Wang, W. Y. Jiang, X. F. Huang, Warming-induced northwestward migration of the East Asian monsoon rain belt from the Last Glacial Maximum to the mid-Holocene. *Proc. Natl. Acad. Sci. U.S.A.* **112**, 13178–13183 (2015).
10. Y. Goldsmith, W. S. Broecker, H. Xu, P. J. Polissar, P. B. de Menocal, N. Porat, J. Lan, P. Cheng, W. Zhou, Z. An, Northward extent of East Asian monsoon covaries with intensity on orbital and millennial timescales. *Proc. Natl. Acad. Sci. U.S.A.* **114**, 1817–1821 (2017).
11. X. F. Huang, S. L. Yang, A. Haywood, D. B. Jiang, Y. D. Wang, M. M. Sun, Z. H. Tang, Z. L. Ding, Warming-induced northwestward migration of the asian summer monsoon in the geological past: Evidence from climate simulations and geological reconstructions. *J. Geophys. Res. Atmos.* **126**, e2021JD035190 (2021).
12. P. U. Clark, J. D. Shakun, P. A. Baker, P. J. Bartlein, S. Brewer, E. Brook, A. E. Carlson, H. Cheng, D. S. Kaufman, Z. Y. Liu, T. M. Marchitto, A. C. Mix, C. Morrill, B. L. Otto-Bliesner, K. Pahnke, J. M. Russell, C. Whitlock, J. F. Adkins, J. L. Blois, J. Clark, S. M. Colman, W. B. Curry, B. P. Flower, F. He, T. C. Johnson, J. Lynch-Stieglitz, V. Markgraf, J. McManus, J. X. Mitrovica, P. I. Moreno, J. W. Williams, Global climate evolution during the last deglaciation. *Proc. Natl Acad. Sci. USA.* **109**, E1134–E1142 (2012).
13. Past Interglacials Working Group of PAGES, Interglacials of the last 800,000 years. *Rev Geophys.* **54**, 162–219 (2016).
14. T. Liu, Loess and the Environment (Science Press, 1985).
15. Z. T. Guo, W. F. Ruddiman, Q. Z. Hao, H. B. Wu, Y. S. Qiao, R. X. Zhu, S. Z. Peng, J. J. Wei, B. Y. Yuan, T. S. Liu, Onset of Asian desertification by 22 Myr ago inferred from loess deposits in China. *Nature* **416**, 159–163 (2002).
16. B. A. Maher, R. Thompson, L. P. Zhou, Spatial and temporal reconstructions of changes in the Asian palaeomonsoon: A new mineral magnetic approach. *Earth Planet. Sci. Lett.* **125**, 461–471 (1994).
17. W. Zhou, F. Xian, Y. Du, X. Kong, Z. Wu, The last 130 ka precipitation reconstruction from Chinese loess ^{10}Be. *J. Geophys. Res. Solid Earth* **119**, 191–197 (2014).
18. J. W. Beck, W. J. Zhou, C. Li, Z. K. Wu, L. White, F. Xian, X. H. Kong, Z. S. An, A 550,000-year record of East Asian monsoon rainfall from10Be in loess. *Science* **360**, 877–881 (2018).
19. T. Li, F. Liu, H. A. Abels, C. You, Z. K. Zhang, J. Chen, J. F. Ji, L. F. Li, L. Li, H. Liu, C. Ren, R. Y. Xia, L. Zhao, W. F. Zhang, G. J. Li, Continued obliquity pacing of East Asian summer precipitation after the mid-Pleistocene transition. *Earth Planet. Sci. Lett.* **457**, 181–190 (2017).

20. X. Q. Meng, L. W. Liu, X. C. T. Wang, W. Balsam, J. Chen, J. F. Ji, Mineralogical evidence of reduced East Asian summer monsoon rainfall on the Chinese loess plateau during the early Pleistocene interglacials. *Earth Planet. Sci. Lett.* **486**, 61–69 (2018).
21. Y. Sun, Q. Yin, M. Crucifix, S. C. Clemens, P. Araya-Melo, W. Liu, X. Qiang, Q. Liu, H. Zhao, L. Liang, H. Chen, Y. Li, L. Zhang, G. Dong, M. Li, W. Zhou, A. Berger, Z. An, Diverse manifestations of the mid-Pleistocene climate transition. *Nat. Commun.* **10**, 352 (2019).
22. F. Peterse, M. A. Prins, C. J. Beets, S. R. Troelstra, H. B. Zheng, Z. Y. Gu, S. Schouten, J. S. S. Damste, Decoupled warming and monsoon precipitation in East Asia over the last deglaciation. *Earth Planet. Sci. Lett.* **301**, 256–264 (2011).
23. H. Yang, R. D. Pancost, X. Y. Dang, X. Y. Zhou, R. P. Evershed, G. Q. Xiao, C. Y. Tang, L. Gao, Z. T. Guo, S. C. Xie, Correlations between microbial tetraether lipids and environmental variables in Chinese soils: Optimizing the paleo-reconstructions in semi-arid and arid regions. *Geochim. Cosmochim. Acta* **126**, 49–69 (2014).
24. E. K. Thomas, S. C. Clemens, Y. B. Sun, Y. S. Huang, W. Prell, G. S. Chen, Z. Y. Liu, S. Loomis, Midlatitude land surface temperature impacts the timing and structure of glacial maxima. *Geophys. Res. Lett.* **44**, 984–992 (2017).
25. C. Y. Tang, H. Yang, R. D. Pancost, M. L. Griffiths, G. Q. Xiao, X. Y. Dang, S. C. Xie, Tropical and high latitude forcing of enhanced megadroughts in Northern China during the last four terminations. *Earth Planet. Sci. Lett.* **479**, 98–107 (2017).
26. H. X. Lu, W. Liu, H. Yang, H. Wang, Z. Liu, Q. Leng, Y. Sun, W. Zhou, Z. An, 800-kyr land temperature variations modulated by vegetation changes on Chinese Loess Plateau. *Nat. Commun.* **10**, 1958 (2019).
27. H. Wang, Z. An, H. Lu, Z. Zhao, W. Liu, Calibrating bacterial tetraether distributions towards in situ soil temperature and application to a loess-paleosol sequence. *Quat. Sci. Rev.* **231**, 106172 (2020).
28. U. Schwertmann, Occurrence and formation of iron oxides in various pedoenvironments, in *Iron in Soils and Clay Minerals*, J. W. Stucki, B. A. Goodman, U. Schwertmann, Eds. (Springer Netherlands 1985), pp. 267–308.
29. R. M. Cornell, U. Schwertmann, *The Iron Oxides: Structure, Properties, Reactions, Occurrences, and Uses*, vol. 2, (Wiley-VCH, 2003), p. 71.
30. X. B. Gao, Q. Z. Hao, L. Wang, F. Oldfield, J. Bloemendal, C. L. Deng, Y. Song, J. Y. Ge, H. B. Wu, B. Xu, F. J. Li, L. Han, Y. Fu, Z. T. Guo, The different climatic response of pedogenic hematite and ferrimagnetic minerals: Evidence from particle-sized modern soils over the Chinese Loess Plateau. *Quat. Sci. Rev.* **179**, 69–86 (2018).
31. Z. L. Ding, E. Derbyshire, S. L. Yang, Z. W. Yu, S. F. Xiong, T. S. Liu, Stacked 2.6-Ma grain size record from the Chinese loess based on five sections and correlation with the deep-sea δ^{18}O record. *Paleoceanography* **17**, 5–1–5–21 (2002).
32. E. Cabello, M. P. Morales, C. J. Serna, V. Barrón, J. Torrent, Magnetic enhancement during the crystallization of ferrihydrite at 25 and 50°C. *Clays Clay Miner.* **57**, 46–53 (2009).
33. F. M. Michel, V. Barrón, J. Torrent, M. P. Morales, C. J. Serna, J. F. Boily, Q. S. Liu, A. Ambrosini, A. C. Cismasu, G. E. Brown Jr., Ordered ferrimagnetic form of ferrihydrite reveals links among structure, composition, and magnetism. *Proc. Natl. Acad. Sci. U.S.A.* **107**, 2787–2792 (2010).
34. Z. X. Jiang, Q. S. Liu, A. P. Roberts, V. Barrón, J. Torrent, Q. Zhang, A new model for transformation of ferrihydrite to hematite in soils and sediments. *Geology* **46**, 987–990 (2018).
35. Z. An, G. J. Kukla, S. C. Porter, J. Xiao, Magnetic susceptibility evidence of monsoon variation on the Loess Plateau of central China during the last 130,000 years. *Quatern. Res.* **36**, 29–36 (1991).
36. Y. Song, Q. Z. Hao, J. Y. Ge, D. A. Zhao, Y. Zhang, Q. Li, X. X. Zuo, Y. W. Lü, P. Wang, Quantitative relationships between magnetic enhancement of modern soils and climatic variables over the Chinese Loess Plateau. *Quat. Int.* **334–335**, 119–131 (2014).
37. J. Jouzel, V. Masson-Delmotte, O. Cattani, G. Dreyfus, S. Falourd, G. Hoffmann, B. Minster, J. Nouet, J. M. Barnola, J. Chappellaz, H. Fischer, J. C. Gallet, S. Johnsen, M. Leuenberger, L. Loulergue, D. Luethi, H. Oerter, F. Parrenin, G. Raisbeck, D. Raynaud, A. Schilt, J. Schwander, E. Selmo, R. Souchez, R. Spahni, B. Stauffer, J. P. Steffensen, B. Stenni, T. F. Stocker, J. L. Tison, M. Werner, E. W. Wolff, Orbital and millennial Antarctic climate variability over the past 800,000 years. *Science* **317**, 793–796 (2007).
38. J. H. F. Jansen, A. Kuijpers, S. R. Troelstra, A mid-Brunhes climatic event: Long-term changes in global atmosphere and ocean circulation. *Science* **232**, 619–622 (1986).
39. I. Candy, G. R. Coope, J. R. Lee, S. A. Parfitt, R. C. Preece, J. Rose, D. C. Schreve, Pronounced warmth during early Middle Pleistocene interglacials: Investigating the Mid-Brunhes Event in the British terrestrial sequence. *Earth Sci. Rev.* **103**, 183–196 (2010).
40. Q. Z. Yin, Insolation-induced mid-Brunhes transition in Southern Ocean ventilation and deep-ocean temperature. *Nature* **494**, 222–225 (2013).
41. J. D. Shakun, D. W. Lea, L. E. Lisiecki, M. E. Raymo, An 800-kyr record of global surface oceanδ18Oand implications for ice volume-temperature coupling. *Earth Planet. Sci. Lett.* **426**, 58–68 (2015).
42. A. A. Prokopenko, D. F. Williams, M. I. Kuzmin, E. B. Karabanov, G. K. Khursevich, J. A. Peck, Muted climate variations in continental Siberia during the mid-Pleistocene epoch. *Nature* **418**, 65–68 (2002).
43. H. Y. Lü, N. Q. Wu, K. B. Liu, H. Jiang, T. S. Liu, Phytoliths as quantitative indicators for the reconstruction of past environmental conditions in China II: Palaeoenvironmental reconstruction in the Loess Plateau. *Quat. Sci. Rev.* **26**, 759–772 (2007).
44. F. Peterse, A. Martínez-García, B. Zhou, C. J. Beets, M. A. Prins, H. Zheng, T. I. Eglinton, Molecular records of continental air temperature and monsoon precipitation variability in East Asia spanning the past 130,000 years. *Quat. Sci. Rev.* **83**, 76–82 (2014).
45. C. W. Snyder, Evolution of global temperature over the past two million years. *Nature* **538**, 226–228 (2016).
46. Q. Z. Hao, L. Wang, F. Oldfield, S. Z. Peng, L. Qin, Y. Song, B. Xu, Y. S. Qiao, J. Bloemendal, Z. T. Guo, Delayed build-up of Arctic ice sheets during 400,000-year minima in insolation variability. *Nature* **490**, 393–396 (2012).
47. P. U. Clark, R. B. Alley, D. Pollard, Northern Hemisphere ice-sheet influences on global climate change. *Science* **286**, 1104–1111 (1999).
48. P. X. Wang, Response of Western Pacific marginal seas to glacial cycles: Paleoceanographic and sedimentological features. *Mar. Geol.* **156**, 5–39 (1999).
49. D. Jiang, Z. Tian, X. Lang, M. Kageyama, G. Ramstein, The concept of global monsoon applied to the last glacial maximum: A multi-model analysis. *Quat. Sci. Rev.* **126**, 126–139 (2015).
50. J. Cao, B. Wang, J. Liu, Attribution of the Last Glacial Maximum climate formation. *Climate Dynam.* **53**, 1661–1679 (2019).
51. N. Wang, D. Jiang, X. Lang, Northern westerlies during the Last Glacial Maximum: Results from CMIP5 simulations. *J. Climate* **31**, 1135–1153 (2018).
52. J. T. Abell, G. Winckler, R. F. Anderson, T. D. Herbert, Poleward and weakened westerlies during Pliocene warmth. *Nature* **589**, 70–75 (2021).
53. U. Herzschuh, X. Cao, T. Laepple, A. Dallmeyer, R. J. Telford, J. Ni, F. Chen, Z. Kong, G. Liu, K. B. Liu, X. Liu, M. Stebich, L. Tang, F. Tian, Y. Wang, J. Wischnewski, Q. Xu, S. Yan, Z. Yang, G. Yu, Y. Zhang, Y. Zhao, Z. Zheng, Position and orientation of the westerly jet determined Holocene rainfall patterns in China. *Nat. Commun.* **10**, 2376 (2019).
54. E. J. Colville, A. E. Carlson, B. L. Beard, R. G. Hatfield, J. S. Stoner, A. V. Reyes, D. J. Ullman, Sr-Nd-Pb isotope evidence for ice-sheet presence on southern Greenland during the Last Interglacial. *Science* **333**, 620–623 (2011).
55. A. V. Reyes, A. E. Carlson, B. L. Beard, R. G. Hatfield, J. S. Stoner, K. Winsor, B. Welke, D. J. Ullman, South Greenland ice-sheet collapse during marine isotope stage 11. *Nature* **510**, 525–528 (2014).
56. R. G. Hatfield, A. V. Reyes, J. S. Stoner, A. E. Carlson, B. L. Beard, K. Winsor, B. Welke, Interglacial responses of the southern Greenland ice sheet over the last 430,000 years determined using particle-size specific magnetic and isotopic tracers. *Earth Planet. Sci. Lett.* **454**, 225–236 (2016).
57. N. Irvalı, E. V. Galaasen, U. S. Ninnemann, Y. Rosenthal, A. Born, H. K. F. Kleiven, A low climate threshold for south Greenland Ice Sheet demise during the Late Pleistocene. *Proc. Natl. Acad. Sci. U.S.A.* **117**, 190–195 (2020).
58. Y. Sui, X. Lang, D. Jiang, Temperature and precipitation signals over China with a 2°C global warming. *Climate Res.* **64**, 227–242 (2015).
59. T. Wang, J. P. Miao, J. Q. Sun, Y. H. Fu, Intensified East Asian summer monsoon and associated precipitation mode shift under the 1.5°C global warming target. *Adv. Clim. Chang. Res.* **9**, 102–111 (2018).
60. F. Tian, B. Dong, J. Robson, R. Sutton, S. F. Tett, Projected near term changes in the East Asian summer monsoon and its uncertainty. *Environ. Res. Lett.* **14**, 084038 (2019).
61. S. Y. Wu, Y. Wu, J. Wen, Future changes in precipitation characteristics in China. *Int. J. Clim.* **39**, 3558–3573 (2019).
62. L. Guo, Z. Jiang, D. Chen, H. Le Treut, L. Li, Projected precipitation changes over China for global warming levels at 1.5°C and 2°C in an ensemble of regional climate simulations: Impact of bias correction methods. *Clim. Change.* **162**, 623–643 (2020).
63. S. C. Porter, Z. S. An, Correlation between climate events in the North Atlantic and China during the last glaciation. *Nature* **375**, 305–308 (1995).
64. C. Scheinost, A. Chavernas, V. Barrón, J. Torrent, Use and limitations of second-derivative diffuse reflectance spectroscopy in the visible to near-infrared range to identify and quantify Fe oxide minerals in soils. *Clays Clay Miner.* **46**, 528–536 (1998).
65. P. O. Mehra, M. L. Jackson, Iron oxide removal from soils and clays by a dithionite-citrate system buffered with sodium bicarbonate. *Clays Clay Miner.* **7**, 317–327 (2013).
66. Ø. Hammer, D. A. Harper, P. D. Ryan, PAST: Paleontological statistics software package for education and data analysis. *Palaeontol. Electron.* **4**, 1–9 (2001).
67. S. E. Fick, R. J. Hijmans, WorldClim 2: New 1-km spatial resolution climate surfaces for global land areas. *Int. J. Climatol.* **37**, 4302–4315 (2017).
68. J. Laskar, F. Joutel, F. Boudin, Orbital, precessional, and insolation quantities for the Earth from −20 Myr to +10 Myr. *Astron. Astrophys.* **270**, 522–533 (1993).
69. B. Bereiter, S. Eggleston, J. Schmitt, C. Nehrbass-Ahles, T. F. Stocker, H. Fischer, S. Kipfstuhl, J. Chappellaz, Revision of the EPICA Dome C CO2record from 800 to 600 kyr before present. *Geophys. Res. Lett.* **42**, 542–549 (2015).
70. L. E. Lisiecki, M. E. Raymo, A Pliocene-Pleistocene stack of 57 globally distributed benthic δ^{18}O records. *Paleoceanography* **20**, 10.1029/2004PA001071 (2005).
71. R. M. Spratt, L. E. Lisiecki, A Late Pleistocene sea level stack. *Clim. Past.* **12**, 1079–1092 (2016).

72. J. Ji, W. Balsam, J. Chen, Mineralogic and climatic interpretations of the Luochuan loess section (China) based on diffuse reflectance spectrophotometry. *Quatern. Res.* **56**, 23–30 (2001).
73. W. Balsam, J. Ji, J. Chen, Climatic interpretation of the Luochuan and Lingtai loess sections, China, based on changing iron oxide mineralogy and magnetic susceptibility. *Earth Planet. Sci. Lett.* **223**, 335–348 (2004).
74. J. Torrent, Q. Liu, J. Bloemendal, V. Barrón, Magnetic enhancement and iron oxides in the upper Luochuan loess–paleosol Sequence, Chinese Loess Plateau. *Soil Sci. Soc. Am. J.* **71**, 1570–1578 (2007).
75. Q. Hao, F. Oldfield, J. Bloemendal, J. Torrent, Z. Guo, The record of changing hematite and goethite accumulation over the past 22 Myr on the Chinese Loess Plateau from magnetic measurements and diffuse reflectance spectroscopy. *J. Geophys. Res. Solid Earth.* **114**, 10.1029/2009JB006604 (2009).
76. Q. S. Liu, J. Torrent, V. Barrón, Z. Q. Duan, J. Bloemendal, Quantification of hematite from the visible diffuse reflectance spectrum: Effects of aluminium substitution and grain morphology. *Clay Miner.* **46**, 137–147 (2011).
77. P. Hu, Z. Jiang, Q. Liu, D. Heslop, A. P. Roberts, J. Torrent, V. Barrón, Estimating the concentration of aluminum-substituted hematite and goethite using diffuse reflectance spectrometry and rock magnetism: Feasibility and limitations. *J. Geophys. Res. Solid Earth.* **121**, 4180–4194 (2016).
78. X. B. Gao, Q. Z. Hao, Y. S. Qiao, S. Z. Peng, N. Li, W. Zhang, L. Han, C. L. Deng, S. B. Marković, Z. T. Guo, Precipitation thresholds for iron oxides dissolution and the enhanced Eurasian aridity across the Mid-Pleistocene Transition: Evidence from loess deposits in subtropical China. *Glob. Planet. Change* **204**, 103580 (2021).
79. C. J. Lepre, P. E. Olsen, Hematite reconstruction of Late Triassic hydroclimate over the Colorado Plateau. *Proc. Natl. Acad. Sci. U.S.A.* **118**, e2004343118 (2021).
80. T. Chen, Q. Xie, H. Xu, J. Chen, J. Ji, H. Lu, W. Balsam, Characteristics and formation mechanism of pedogenic hematite in Quaternary Chinese loess and paleosols. *Catena* **81**, 217–225 (2010).

Acknowledgments: We thank F. Li for assistance in collecting the modern soils, S. Liu, Z. Jiang, and Q. Zhang for help with laboratory measurements, and C. Tan, Q. Jiang, H. Lu, N. Namier, and H. Zhang for helpful discussions. **Funding:** This work is funded by the National Natural Science Foundation of China (41888101, to Z.G.), National Natural Science Foundation of China (41625010, to Q.H.), National Natural Science Foundation of China (42007399, to X.G.), and the Strategic Priority Research Program of the Chinese Academy of Sciences (XDB26000000, to Q.H.). **Author contributions:** Conceptualization: Q.H. and Z.G. Investigation: X.G., Q.H., Y.S., J.G., B.X., L.H., Y.F., X.W., C.D., and Z.G. Writing—original draft: X.G. and Q.H. Writing—review and editing: X.G., Q.H., H.W., L.H., Y.F., and C.D. Methodology: X.G., Q.H., and L.W. Resources: X.G., Q.H., Y.S., J.G., H.W., B.X., and Z.G. Data curation: X.G. and Q.H. Supervision: X.G., Q.H., Y.F., and Z.G. Project administration: Z.G., Q.H., and X.G. Funding acquisition: Z.G. and X.G. Formal analysis: X.G., Q.H., L.W., H.W., and L.H. Software: Q.H. and L.W. Visualization: X.G. and Q.H. Validation: X.G., Q.H., B.X., and L.H. **Competing interests:** The authors declare that they have no competing interests. **Data and materials availability:** All data needed to evaluate the conclusions in the paper are present in the paper and/or the Supplementary Materials. Data are also available at the online data repository figshare (https://doi.org/10.6084/m9.figshare.25263637.v1).

Submitted 7 November 2023
Accepted 10 April 2024
Published 15 May 2024
10.1126/sciadv.adm7694